Materialia 9 (2020) 100524

Contents lists available at ScienceDirect

Materialia

journal homepage: www.elsevier.com/locate/mtla

Full Length Article

Hydrogen embrittlement in super duplex stainless steels

X.Z. Liang[a,b], G.-H. Zhao[a], M.F. Dodge[c], T.L. Lee[d], H.B. Dong[b,*], P.E.J. Rivera-Díaz-del-Castillo[a,*]

[a] Department of Engineering, Lancaster University, Lancaster LA1 4YW, UK
[b] Department of Engineering, University of Leicester, Leicester LE1 7RH, UK
[c] TWI Ltd., Cambridge CB21 6AL, UK
[d] ISIS Neutron Source, Science and Technology Facilities Council, Rutherford Appleton Laboratory, Oxford OX11 0QX, UK

ARTICLE INFO

Keywords:
Hydrogen embrittlement
Crack propagation
Neutron diffraction
Super duplex stainless steel (SDSS)

ABSTRACT

In super duplex stainless steels (SDSSs), both austenite and ferrite are susceptible to hydrogen embrittlement, however there is a lack of understanding into the effect of hydrogen in each phase. In this study, in neutron diffraction was applied on hydrogen-charged (H-charged) samples to investigate the hydrogen embrittlement behaviour in super duplex stainless steels. The result reveals that austenite maintains good plasticity during tensile testing, whilst a loss of it is realised in ferrite. Fractography analysis reveals the diffusion of hydrogen induced a brittle-to-ductile transition from the sample surface towards the centre; hydrogen embrittlement vanishes as the specimen's centre is approached, while it is demonstrated to disappear first in austenite but not in ferrite. This transition can be predicted by applying a physics-based hydrogen embrittlement model which incorporates the effects of hydrogen concentration, hydrogen diffusivity, residual stress, loading state and temperature. The present work demonstrates the dissimilar susceptibility of austenite and ferrite to hydrogen embrittlement, providing a tool to describe it.

1. Introduction

Super duplex stainless steels (SDSSs) possess a balanced microstructure of ferrite (δ) and austenite (γ) [1–5]. Such mix provides good corrosion resistance and merit mechanical properties [2–7], making SDSSs widely used in industry, e.g. in onshore refineries and offshore pipelines. However, the mechanical properties of SDSSs can be degraded by hydrogen. It has been widely reported that upon reaching a critical concentration of solute hydrogen, the materials' plasticity loss can be realised and can result in premature failure [8–17]. Such phenomenon is termed hydrogen embrittlement (HE).

Several established mechanisms have been proposed to account for HE, such as hydride-induced embrittlement [18,19], hydrogen enhanced decohesion (HEDE) [20–25] and hydrogen enhanced local plasticity (HELP) [26–31]. Hydride-induced embrittlement is only observed in special circumstances [18,19], and is not thought to be a general mechanism of HE in steels. The mechanism of HEDE proposes that hydrogen can lead to a weakening of the lattice coherent bonding, thus facilitating crack initiation and propagation. The HELP mechanism was proposed based on the direct observation of dislocation pile-ups within a hydrogen atmosphere using an environmental transmission electron microscopy (TEM) [26,27], and a high density of slips lines at the vicinity of the fractured region [29]. These observations show local plasticity can be enhanced with solute hydrogen. A key principle behind HELP is the dislocation-dislocation shielding mechanism; this arises as hydrogen enters the stress field near an edge dislocation, lowering the magnitude of the field, and leading to a decrease in dislocation-dislocation interaction strength [31]. Micromechanical modelling has indicated hydrogen trapping near dislocations in steel leads to a decrease in such dislocation interaction.

HE becomes more complicated in dual-phase materials. With recent advances in characterisation techniques, more hydrogen-metal interactions in dual-phase materials have been reported. By applying *in-situ* tensile test in a SEM, Koyama et al. [32] reported that hydrogen can facilitate an unhomogenized plasticity evolution in dual phase steels. Örnek et al. [33] investigated the load partitioning in super duplex stainless steels using digital imaging correlation. In hydrogen-free sample, the result shows that ferrite grains carry a higher load than austenite grains; whilst in hydrogen pre-charged sample, the austenite grains carry higher load compared with ferrite grains. Nevertheless, there is a limit that these results were characterised from the surface where the bulk information cannot be probed. Neutron has a high penetration and the neutron diffraction has been increasingly used to investigate the microstructure in bulk materials in recent decades [34–36]. Thus, this technique was used in this study to study the microstructural evolution in bulk SDSSs.

In SDSSs, ferrite has a high hydrogen diffusivity and a low hydrogen solubility; conversely, austenite possess low hydrogen diffusivity and high hydrogen solubility [37,38]. Therefore, in SDSSs, ferrite is likely

* Corresponding authors.
E-mail addresses: h.dong@le.ac.uk, p.rivera1@lancaster.ac.uk (H.B. Dong), p.rivera1@lancaster.ac.uk (P.E.J. Rivera-Díaz-del-Castillo).

https://doi.org/10.1016/j.mtla.2019.100524
Received 24 October 2019; Accepted 1 November 2019
Available online 5 November 2019

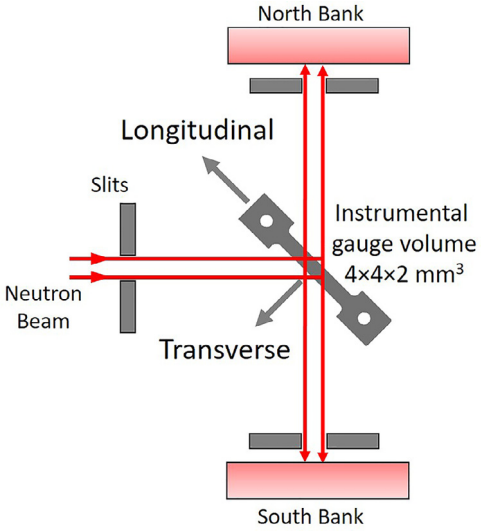

Fig. 1. Schematic representation of the neutron diffraction experiment setup.

act as a path to transport hydrogen whilst austenite is a sink, trapping it. In terms of hydrogen assisted cracking in SDSSs, it has been shown that hydrogen assisted cracks mostly arise from ferrite and get trapped in austenite, which suggests that ferrite has lower resistance to hydrogen embrittlement than austenite [33,39]. However, it is a challenge to quantitatively model the hydrogen embrittlement in the duplex stainless steels, as the nucleation and propagation of hydrogen assisted cracking occurs in ferrite and austenite. Song and Curtin [40] proposed a prototype which can model the hydrogen embrittlement in iron. Based on that, in this study, a hydrogen embrittlement model is proposed for hydrogen embrittlement in SDSSs which incorporates the effects of hydrogen concentration, hydrogen diffusivity, residual stress, loading state and temperature.

2. Experimental methods

2.1. Materials

Specimen materials were taken from a UNS S32760 pipeline. The measured chemical composition of which (in weight percent) is 0.032%C, 0.54%Si, 0.72%Mn, 0.019%P, 0.009%S, 25.1%Cr, 3.56%Mo, 7.0%Ni, 0.01%Al, 0.01%As, 0.080%Co, 0.820%Cu, 0.040%Nb, 0.005%Sn, 0.007%Ti, 0.050%V, 0.680%W, 0.270%N with Fe balance. Solution heat treatment was performed at 1200° C for 1 h followed by water quenching. This heat treatment was applied to remove residual stresses and homogenise the microstructure. Tensile samples with a gauge volume of $35\times5\times1.2$ mm^3 were prepared. Surfaces were ground with emery sand paper up to 1200 grit. A cathodic charging cell was used for hydrogen charging: samples were connected to cathodic lead and immersed into a 3.5 wt% NaCl solution at 50° C whilst a platinum wire was used as an anode. A 10 day hydrogen charging was applied with a 10 mA/cm^2 current density before tensile tests. In order to eliminate potential ferrite cracking prior to mechanical tests, the specimens were examined by optical microscopy to confirm the absence of defects induced by H-charging. The surface of electron backscatter diffraction (EBSD) samples was ground down to 0.04 μm, followed by electropolishing using 10 wt.% $HClO_4$ alcohol solution at 45 V potential for 5 s. During electropolishing, the sample was connected to the anode whilst a platinum wire was connected to the cathode.

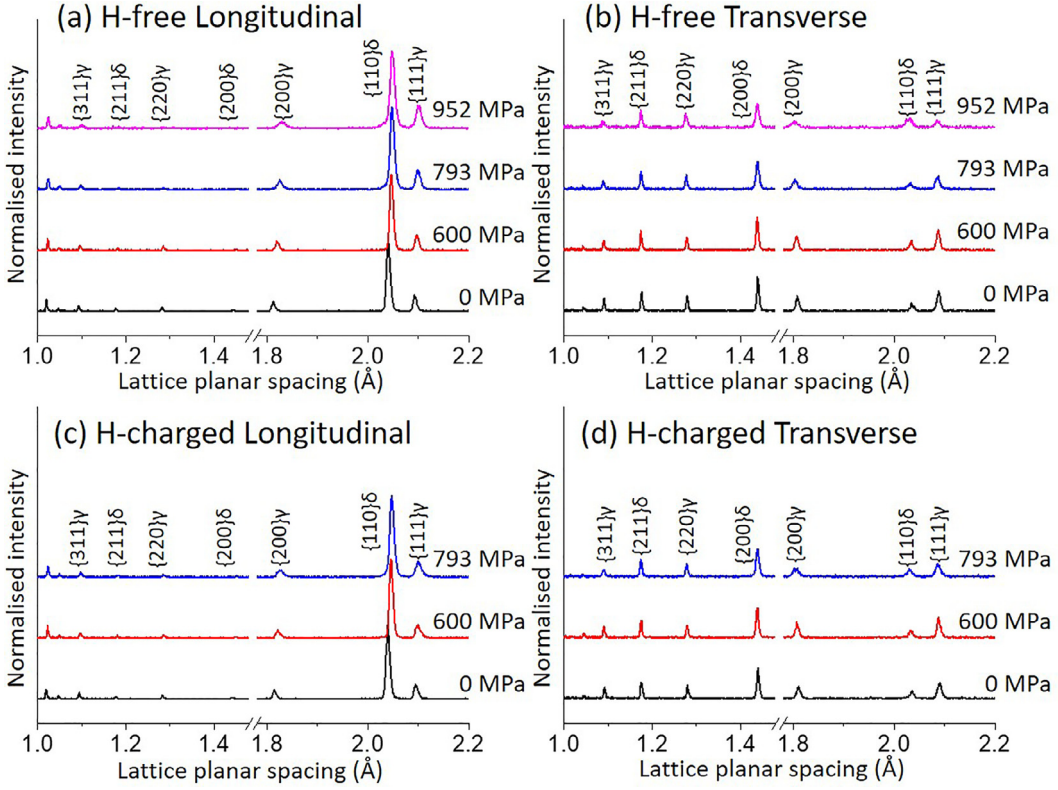

Fig. 2. Neutron diffraction patterns of H-free and H-charged samples at strain rate of 1.0×10^{-4} s^{-1}: (a) and (b) were obtained from H-free sample along longitudinal and transverse directions, respectively; (c) and (d) were obtained from H-charged sample along longitudinal and transverse directions, respectively; both austenite (γ) and ferrite (δ) peaks were identified at stress levels of 0, 600, 793 and 952 MPa.

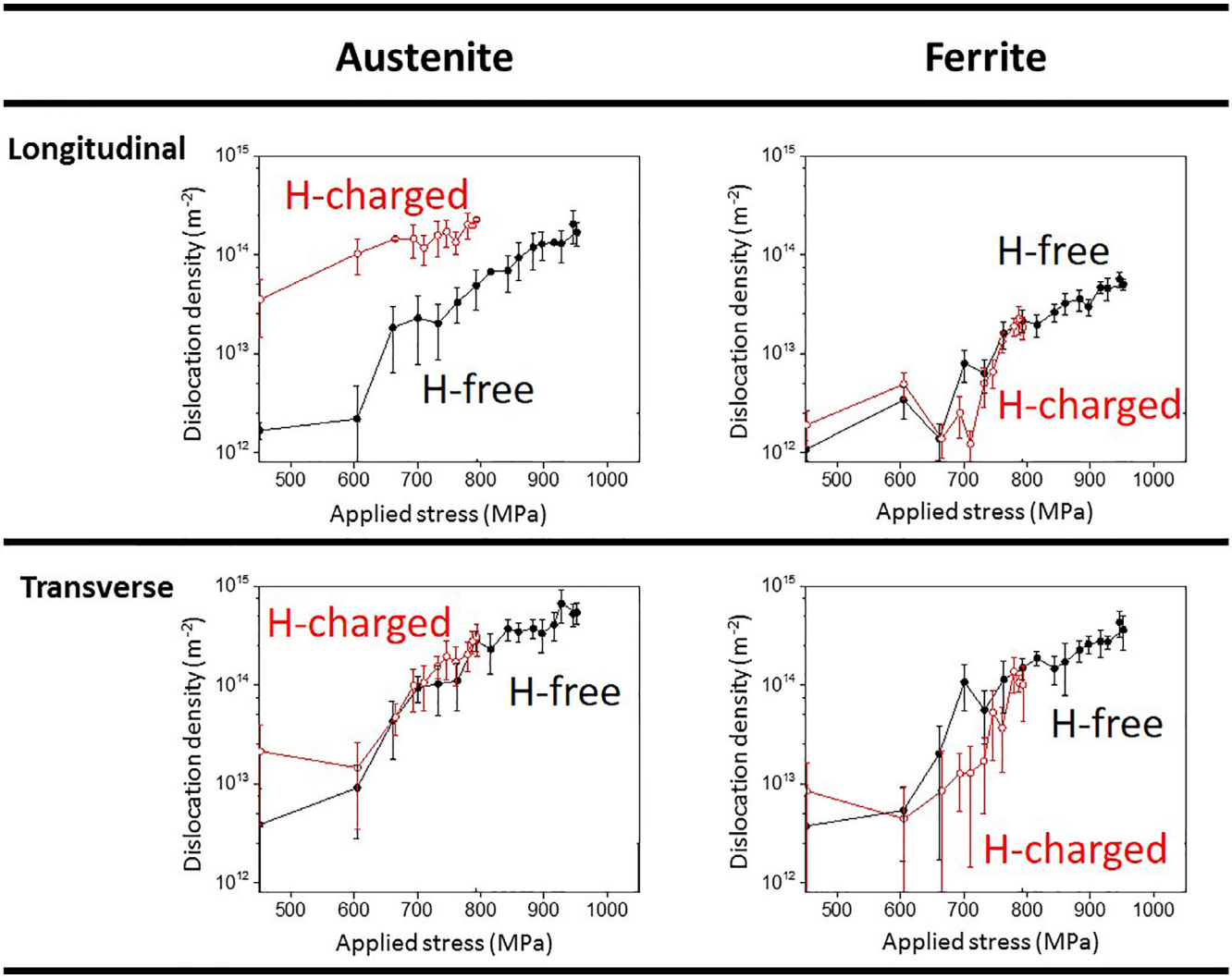

Fig. 3. *In-situ* neutron diffraction results showing evolution of dislocation density in austenite and ferrite; both H-free and H-charged samples were tested at strain rate of 1.0×10^{-4} s^{-1}.

2.2. Tensile tests and characterisations

Tensile tests were performed at room temperature for both H-free and H-charged samples. The H-charged samples immediately underwent uniaxial tensile tests after charging. The tensile tests were performed on an Instron stress rig with a maxium loading capability of 100 kN. Three different strain rates are applied namely 1.0×10^{-2}, 1.0×10^{-3} and 1.0×10^{-4} s^{-1}. Scanning electron microscopy (SEM) was performed on a Tescan Mira 3 at 30 kV coupled with an energy-dispersive X-ray spectroscopy (EDS) detector and an Oxford Instruments EBSD detector. The sample was mounted using a 70° pre-tilt stage in the SEM for EBSD scanning. A scanning scheme of 2×2 camera binning and 100 nm step size was chosen to capture EBSD patterns.

2.3. In-situ neutron diffraction upon tensile testing

2.3.1. Experimental setup

Time-of-flight neutron diffraction experiments were performed on the ENGIN-X neutron diffractometer, ISIS, UK. Fig. 1 shows the schematic diagram of the neutron diffraction setup. The sample was mounted onto an INSTRON stress rig with the sample longitudinal direction oriented horizontally at 45° relative to the incident beam. A $4 \times 4 \times 2$ mm^3 instrumental gauge volume was used (2 mm in the direction normal to the sample) and the diffracted neutrons were collected with detectors fixed at $2\theta = \pm 90°$ to the incident beam. This allows the lattice spacing and the dislocation density data parallel to the sample longitudinal direction to be derived from the data measured by the North detector bank while the South detector bank measured data for the sample transverse direction. An extensometer was mounted onto the sample at the centre of the gauge length section to measure the sample macroscopic strain during tensile testing. Stress control was programmed during elastic deformation, which neutrons are collected at 150, 300, 450 and 600 MPa. Afterwards, strain control was programmed with a strain increment of 0.7% (0.25 mm elongation) for hydrogen-charged samples and 1.4% (0.5 mm elongation) for hydrogen-free samples. A neutron collection time of 8 min was set at each interval.

2.3.2. Dislocation density measurement

The evolution of dislocation density can be measured by obtaining the variation of full width at half maximum (FWHM) [41–43]. In this study, FWHM of each peak was determined from the single-peak fitting method using the OpenGENIE programme with a least squares refinement fit of a pseudo-Voigt function convolved with a leading and trailing exponential function (accounting for the inherent asymmetric diffraction line profiles of the neutron diffraction data). Liang et al. [34] employed neutron diffraction to measure the dislocation density in super duplex stainless steels. In their work, a standard diffraction pattern was obtained in a hydrogen free sample, which was used as a

Table 1
Summary of the mechanical properties in H-free and H-charged samples.

Test No.	H-condition	Strain rate (s^{-1})	Elongation (%)	Yield strength (0.2%, MPa)	UTS (MPa)
1	H-free	1.0×10^{-2}	25.1 ± 1.1	600	988
2		1.0×10^{-3}	24.4 ± 0.9	597	961
3		1.0×10^{-4}	25.5 ± 1.2	602	988
4	H-charged	1.0×10^{-2}	16.6 ± 0.8	646	972
5		1.0×10^{-3}	16.3 ± 0.9	633	1001
6		1.0×10^{-4}	3.6 ± 0.6	630	793

reference pattern. This method is appropriate to measure dislocation densities if a reference diffraction pattern can be obtained from a low dislocation density reference specimen. The following equation was used to derive the dislocation density:

$$\rho = \frac{15E}{2Gb^2(1+\upsilon)}\left(\frac{\Delta d}{d}\right)^2 \quad (1)$$

where E and G are the elastic modulus and the shear modulus, respectively. Typical values of $E/G = 2.5$ and poisson ratio $\upsilon = 0.3$ are used for both austenite and ferrite. b is the magnitude of the Burgers vector, which is estimated to be 0.248 nm for ferrite and 0.254 nm for austenite, respectively [34]. The standard peak width reference was obtained from the hydrogen free sample and an intrinsic 1.0×10^{12} m^{-2} dislocation density was assumed for the standard peak width [34,41]. In this study, we adopt this calculation scheme to measure the evolution of dislocation density during tensile testing.

3. Results

3.1. Evolution of dislocation density during uniaxial tensile test

In-situ neutron diffraction was applied to examine the evolution of dislocation density in both H-charged and H-free samples during tensile tests. Fig. 2 shows neutron diffraction patterns during tensile testing at strain rate of 1.0×10^{-4} s^{-1}. {110}, {200} and {211} planes are identified for ferrite while {111}, {200}, {220} and {311} planes are identified for austenite. During loading, increasing of the lattice planar spacing was observed on the longitudinal direction whilst decreasing of the lattice planar spacing was observed on the transverse direction. This is due to a tensile stress is applied on the longitudinal direction whilst a compressive stress is realised on the transverse direction.

Fig. 3 shows the evolution of dislocation density in both austenite and ferrite upon loading. In the macroscopic elastic region (under 600 MPa), H-charged samples possess higher dislocation density compared with H-free samples in both austenite and ferrite. In austenite, on the longitudinal direction, a dislocation density higher than one order of magnitude was measured in the H-charged sample, whilst the evolution in dislocation multiplication appears not to change in the transverse direction. Delayed dislocation multiplication is observed in ferrite in H-charged samples in both directions. Further discussion is presented in Section 4.3.

3.2. Mechanical properties

Both H-free and H-charged samples underwent tensile tests at strain rates of 1.0×10^{-2}, 1.0×10^{-3} and 1.0×10^{-4} s^{-1}. Fig. 4(a) shows the stress-strain curves and Fig. 4(b) shows each applied strain rate against elongation. Table 1 lists the values of elongation, yield strength and ultimate tensile strength (UTS). The result depicts a higher yield strength obtained in H-charged samples. However, the degradation of elongation is realised in H-charged samples, which indicates a loss of ductility due to hydrogen.

In H-free samples, the tensile test result shows that the variation of strain rates in the range between 1.0×10^{-2} and 1.0×10^{-4} s^{-1} has

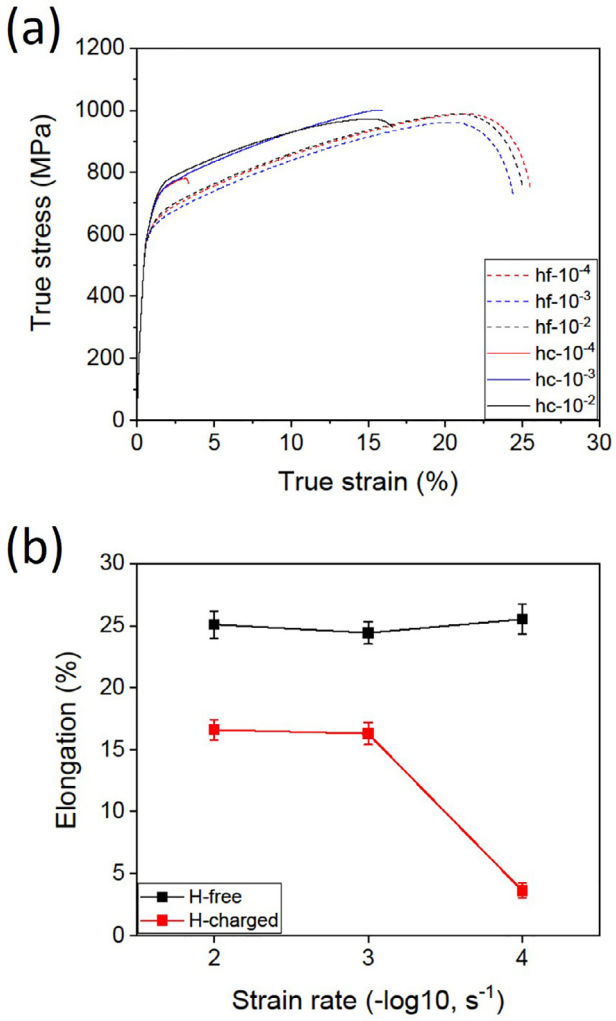

Fig. 4. Tensile results of samples at different strain rate: (a) true stress-strain curves, hf and hc represent H-free and H-charged, respectively; (b) elongation at different strain rate.

Table 2
SEM-EDS measurement of Cr and Ni (wt.%) elements in facet and dimple features.

Elements	Facet	Dimple
Cr (wt.%)	29.5 ± 0.2	27.3 ± 0.2
Ni (wt.%)	5.7 ± 0.2	6.5 ± 0.2

negligible effect on the elongation, yield strength and UTS. However, in H-rich samples, decreases of elongation and reduction of area are realised with the decrease of strain rate. A lowest elongation of 3.6 ± 0.6% was achieved in sample tested at a strain rate of 1.0×10^{-4} s^{-1}, which shows a same trend as reported in reference [44].

3.3. Fractography and characterisation of microcracks

Fig. 5 shows the fractography of H-charged sample at strain rate of 1.0×10^{-4}. A transition of fracture from ductile to brittle is observed. Fig. 6 shows typical high magnification images obtained within the region that has mixture of facet (brittle feature) and dimple (ductile feature). A further EDS chemical composition analysis was performed in facet and dimple regions, as shown in Table 2. A higher chromium and lower nickel content is obtained in the facet region, which suggests a high fraction of ferrite in such area.

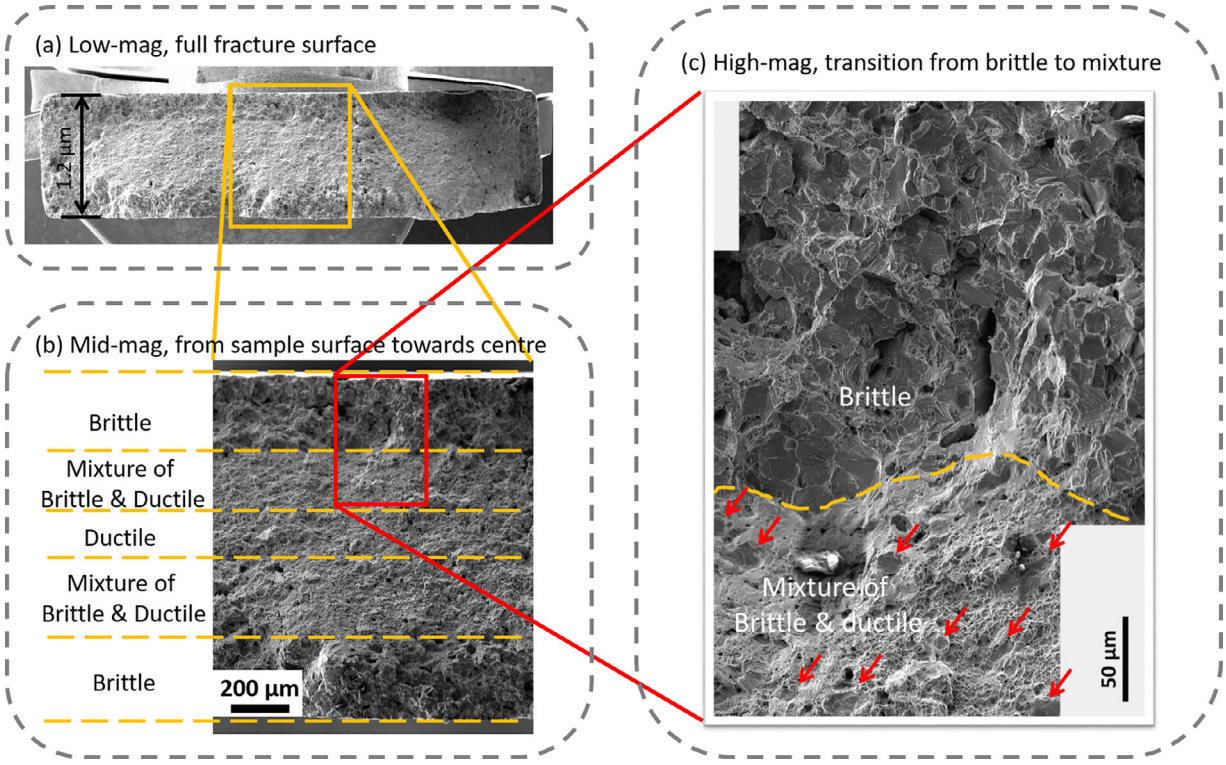

Fig. 5. SEM fractography of H-charged sample at 1.0×10^{-4} strain rate; (a) low-magnification image showing the fracture surface; (b) mid-magnification image showing regions of brittle, mixture of brittle & ductile and ductile along the thickness direction; (c) high-magnification image showing transition from brittle to mixed brittle/ductile regions.

Microcracks are observed on the surface side near the fracture. Fig. 7 shows EBSD characterisation of several microcracks on the side surface of the H-charged sample at a strain rate 1.0×10^{-4} s^{-1}. These intragranular cracks propagate mostly through ferrite and become arrested in austenite, which suggests that ferrite is more prone to HE compared with austenite.

4. Discussion

4.1. H-assisted crack propagation in ferrite and austenite

The fractography results in Section 3.3 demonstrates the presence of H-assisted cleavage fracture in ferrite rather than in austenite. This phenomenon is associated with the difference in crack propagation rate in ferrite compared to austenite. Song et al. [40,45] proposed a criterion to describe the hydrogen embrittlement at the microscale. In hydrogen-rich steels, the rate of crack growth can be estimated by:

$$\alpha = \frac{4}{\pi}\frac{D\omega}{k_B T}\frac{(1+\upsilon)K_I}{3\sqrt{2\pi}}\left(\frac{\pi c_0}{a_0}\right)^{\frac{5}{4}} \triangle l^{-\frac{1}{4}}, \tag{2}$$

where D is the diffusion coefficient of hydrogen in the lattice; ω is the partial volume of hydrogen interstitials in Fe; k_B is the Boltzmann constant; T is the temperature; c_0 is the hydrogen concentration on an Fe atom basis; a_0 is the lattice constant; $\triangle l$ is the length of the growing crack; K_I is the stress intensity field which can be expressed by $K_I = \sigma\sqrt{2\pi l_f}$ where l_f is the effective flaw size.

According to Eq. (2), the growth rate of hydrogen assisted microcracks can be estimated for super duplex stainless steels (SDSSs). Here, a comparison of the crack growth rate in ferrite (δ) and austenite (γ) can be obtained from

$$\frac{\alpha_\delta}{\alpha_\gamma} \cong \frac{D_\delta}{D_\gamma}\frac{\omega_\delta}{\omega_\gamma}\left(\frac{c_{0,\delta}/a_{0,\delta}}{c_{0,\gamma}/a_{0,\gamma}}\right)^{\frac{5}{4}} \tag{3}$$

The diffusivity and solubility of hydrogen in ferrite and austenite behave dramatically different. Literature reported that the diffusion coefficient of hydrogen in ferrite is in the order of 10^{-10}–10^{-11} m^2/s whilst it ranges from 10^{-16} to 8×10^{-16} m^2/s for austenite [37,46]. The partial volume ω of hydrogen in ferrite and austenite are 3.818 [40] and 2.07 $Å^3$ [47], respectively.

The values of $c_{0,\delta}$ and $c_{0,\gamma}$ are reported to be 0.033 ppm and 32.51 ppm, respectively [48]. Thus, the ratio of $\frac{c_{0,\delta}}{c_{0,\gamma}}$ is $\sim 10^{-3}$. The lattice constant for ferrite and austenite are 2.86 and 3.57 Å, respectively. Therefore, the ratio of $\frac{\alpha_\delta}{\alpha_\gamma}$ is estimated to be in the range of 10^2–10^3, which suggests the crack growth rate in ferrite to be much faster than in austenite. Thus, fracture in ferrite is prone to cleavage in SDSSs.

As shown in Fig. 7, the H-assisted cracks propagate through ferrite grains whilst their tips are arrested in austenite. The length of these microcracks is about 10 to 20 µm. Using Eq. (2), crack propagation rate and crack length can be calculated for ferrite and austenite. The following parameters are used for modelling: l_f=10 µm, $D_\delta = 5 \times 10^{11}$ m^2/s and $D_\gamma = 5 \times 10^{16}$ m^2/s. Fig. 8 shows the H-assisted crack growth rate and crack length with the evolution of strain for both ferrite and austenite. The crack growth rate in ferrite is more than a order of magnitude higher than in austenite. After the materials failure at 3.6% elongation, the H-assisted crack length in ferrite can be developed to 20 µm, which is approximately equal to the ferrite grain size. Therefore, it can be proposed that the H-assisted failure could be triggered when cracks propagate across ferrite grains.

4.2. Hydrogen embrittlement in ferrite and austenite

4.2.1. Hydrogen profile in the sample

As shown in Fig. 5, a fracture trasition from brittle to ductile can be observed; this is due to the hydrogen gradient from the sample surface

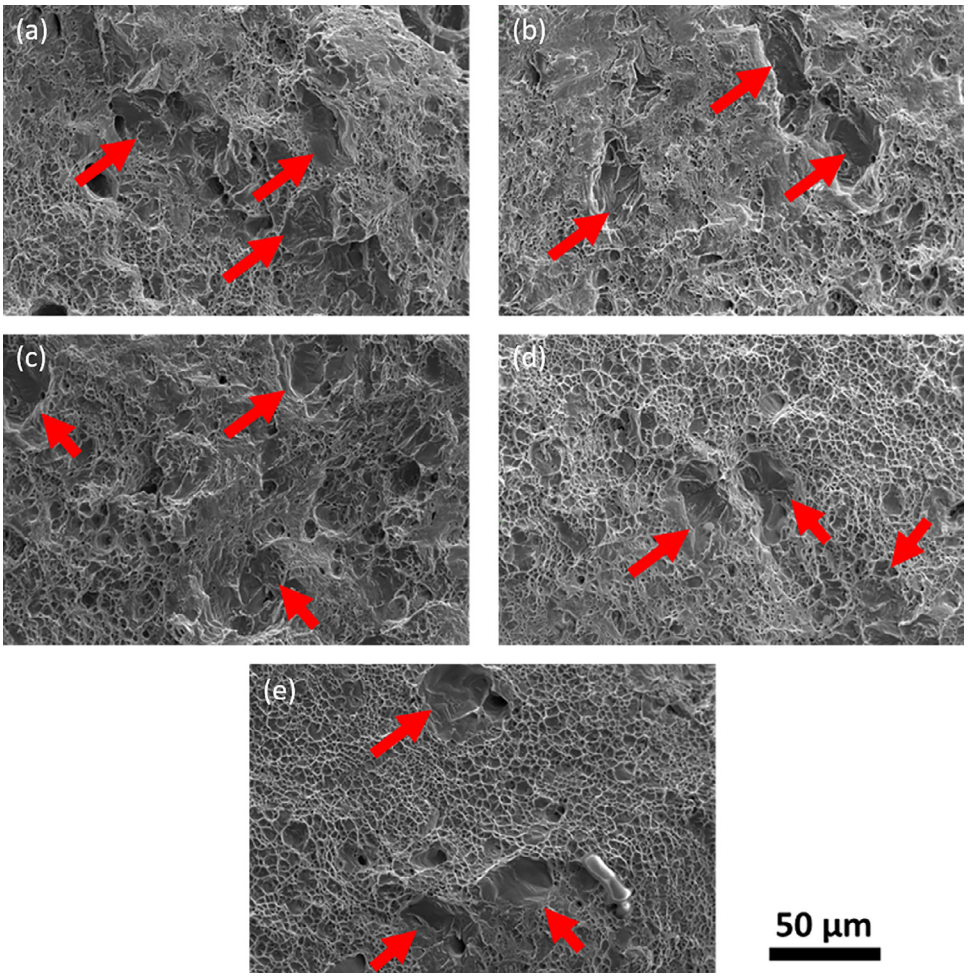

Fig. 6. SEM fractography of H-charged sample showing typical regions (a-e) with mixed brittle and ductile fractures.

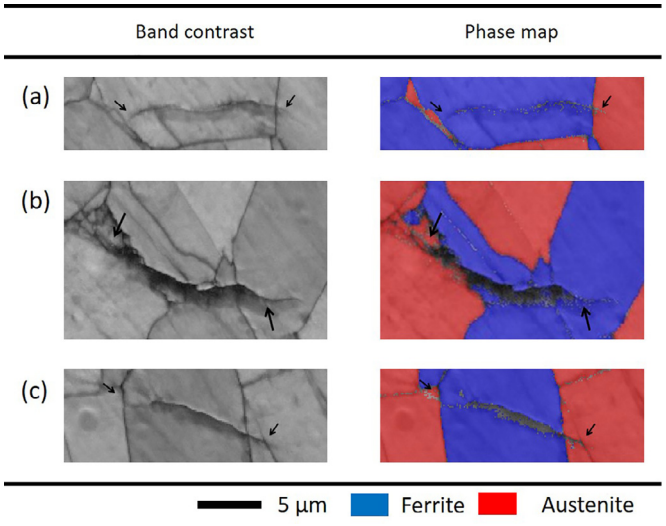

Fig. 7. EBSD characterisation of intragranular microcracks in ferrite on the side surface of H-charged sample; arrows in (a-c) indicate the position of crack tips; uniaxial tensioning was applied vertically at strain rate of 1.0×10^{-4} s^{-1}.

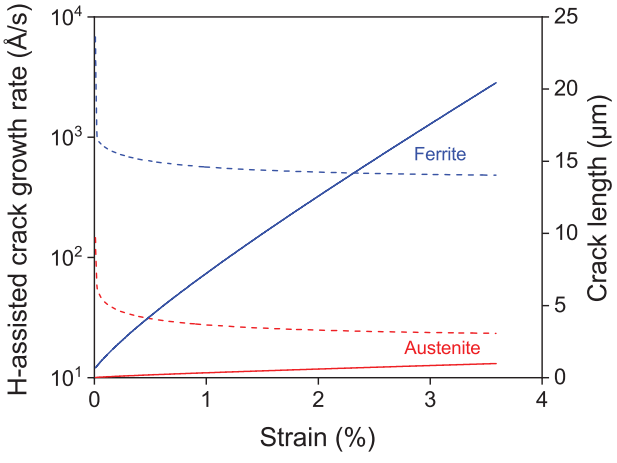

Fig. 8. Modelling of H-assisted cracks propagation in ferrite and austenite; dotted lines represent crack growth rate; solid lines represent accumulated crack length.

towards the centre. If a semi-infinite plate is assumed, the gradient of hydrogen concentration across the thickness can be modelled solving Fick's second law

$$c = c_i + (c_s - c_i)\left\{1 - \mathrm{erf}\left[z/2(Dt)^{\frac{1}{2}}\right]\right\}, \quad (4)$$

where c_i and c_s are the initial hydrogen concentration and saturated hydrogen concentration, respectively; z is the penetration depth whilst t is the diffusion time. For the hydrogen charging condition in this study, the values of c_i and c_s can be defined as 0 and 1, respectively. The penetration depth is half of the sample thickness. The diffusion time is 10 days. At 50° C H-charging environment, the diffusivity can be estimated to be 2×10^{-14} m^2/s. The hydrogen saturation can be calculated

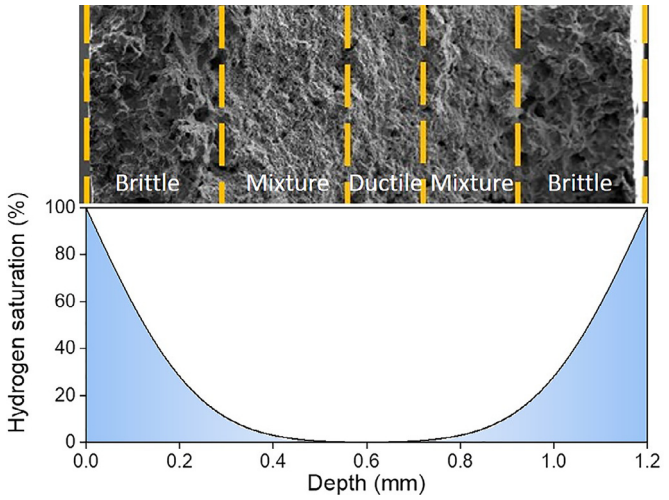

Fig. 9. Modelling hydrogen saturation in the sample after H-charging. The hydrogen diffusivity is $D = 2 \times 10^{-14}$ m^2/s. The corresponding fractography image is placed on top showing that the hydrogen saturation profile has a same trend with the brittle-to-ductile transition in fractography image.

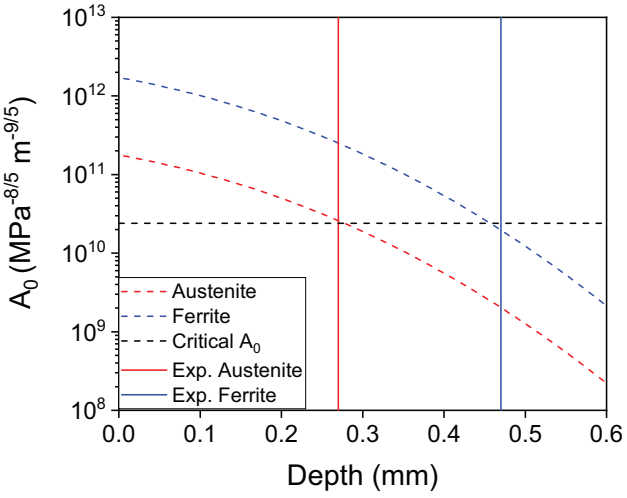

Fig. 10. Modelling the presence of hydrogen embrittlement in terms of hydrogen saturation; HE was absent for depths under 0.27 ± 0.02 mm for austenite and 0.47 ± 0.09 mm for ferrite; a threshold value of approximately 2.4×10^{10} MPa$^{-8/5}$ m$^{-9/5}$ is obtained for A_0 in this study.

by $s = \frac{c}{c_s}$. Fig. 9 shows the hydrogen saturation profile from the surface towards the centre. The result shows a 20% hydrogen saturation can reach ~0.2 mm depth. Here, it should be noted that the estimation of hydrogen concentration is a first order estimation.

4.2.2. Effect of residual stress on hydrogen concentration

The thermal expansion coefficients of ferrite and austenite are different. Therefore, a residual stress can be generated in SDSSs by quenching [38]. The presence of such residual stress has a significant effect on hydrogen concentration in SDSSs. The solubility of hydrogen in the presence of stress can be expressed by

$$C_0^* = C_0 \exp\left(\frac{-\sigma\omega}{k_B T}\right) \tag{5}$$

where C_0 is the concentraton in the stress-free state [4]. Barnoush et al. [4] reported that a compressive residual stress of 400 MPa exists in ferrite whilst a tensile residual stress of 470 MPa is present in austenite. By adopting these values, the solubility of austenite has a 23% increase whilst ferrite has a 36% decrease.

4.2.3. Modelling the presence of hydrogen emrbittlement in SDSSs

The fracture can be clasiffied as ductile or brittle [49]. At the microscale, the classification depends on the feature of the crack tip where a ductile feature is always accompanied by dislocation emission whilst this is absent in brittle fracture. Therefore, a facet feature will be present if H-assited crack growth is dominant, and as its present of facet in fractography is a sign of hydrogen emrbittlement. From the above discussion, the propagation of H-assisted cracking depends on many factors including hydrogen diffusivity, hydrogen concentration, stress state and temperature. Song and Curtin [40] incorporated these factors and then introduced an index A_0 to predict the occurrence of hydrogen emrbittlement. In this study, by considering the hydrogen saturation profile in SDSSs, the following expression can be used to calculate a hydrogen embrittlement index value to predict the hydrogen emrbittlement:

$$A_0 = \beta(0.5, 0.9)\frac{2c_0^* s}{a_0^3}\left(\frac{5(1+\upsilon)D\omega}{12\sqrt{2\pi}k_B T \dot{K}_I}\right)^{\frac{4}{5}} \tag{6}$$

where the term $c_0^* s$ indicates the local hydrogen concentration in austenite or ferrite. Therefore, the A_0 can be calculated for both ferrite and austenite as $A_{0,\delta}$ and $A_{0,\gamma}$, respectively. Fig. 10 shows the evolution of $A_{0,\delta}$ and $A_{0,\gamma}$ as a function of depth in austenite and in ferrite. Experimental results show HE is absent for depths under 0.27 ± 0.02 mm for austenite and 0.47 ± 0.09 mm for ferrite. Therefore, a threshold value of approximately 2.4×10^{10} MPa$^{-8/5}$ m$^{-9/5}$ is obtained in this study to distinguish the HE and ductile feature for both austenite and ferrite. This value is about 5 times less than the value 1.4×10^{11} MPa$^{-8/5}$ m$^{-9/5}$ reported by Song and Curtin [40]. The difference may be due to the complexity of microstructure in SDSSs. Although the residual stresses in both ferrite and austenite have been considered in terms of hydrogen solubility, hydrogen diffusivity can be affected as well. If a higher diffusivity is realised in both ferrite and austenite, a higher A_0 can be predicted which will have better agreement with the value reported by Song and Curtin [40]. Also, the presence of ferrite-austenite phase boundaries has higher hydrogen diffusivity which diffuses hydrogen deeper, and thus the hydrogen emrbittlement can occur deeper in the sample.

4.3. Evolution of dislocation density and load partitioning

A previous study [34] has reported that dislocation multiplication can be activated by hydrogen charging in SDSSs before loading. After hydrogen charging, dislocation densities 1.0×10^{12} m^{-2} of austenite and ferrite are increased to 6.9×10^{12} and 1.7×10^{12} m^{-2}, respectively. The Frank-Read-type source is suggested to account for dislocation density multiplication by hydrogen charging [34]. In this study dislocation multiplication during loading is investigated. Fig. 3 shows the evolution of dislocation density in H-free and H-charged samples. The evolution of dislocation density is facilitated in austenite by hydrogen, which can be expained by hydrogen-hardening in austenite. Therefore, a higher loading partitioning in austenite is realised. This observation matches the report in reference [33] which a higher localized plastic strain was measured in austenite at 1.7% strain in H pre-charged SDSSs. It is worth to note that the H-assisted failure occurred just before a stable evolution of dislocation density in ferrite. This result matches the discussion in Section 4.1 that H-assisted crack propagation is faster in ferrite so that a lose of plasticity of ferrite is realised in the presence of hydrogen.

4.4. Microstructure design to prevent hydrogen embrittlement

In this study, the hydrogen assisted crack propagation rate and the hydrogen embrittlement index value have been expressed via Equation (2) and (6), respectively. These equations incorporate hydrogen diffusivity, hydrogen solubility, residual stress, temperature and load. These outcomes can assist industrial practice to prevent hydrogen

embrittlement in terms of service life prediction, critical load estimations, and microstructural design of duplex stainless steels. For example, state-of-the-art industrial practical guidance to prevent the hydrogen induced stress in duplex stainless steels has been documented in DNVGL-RP-F112 [50]. In terms of microstructure, a finer austenite spacing is desirable, and the primary reason is that the presence of closer austenite grains can effectively blunt the hydrogen-assisted crack tips which initiated from ferrite grains [33]. However, there is a lack of quantitative prediction of service life subject to different levels of austenite spacing. According to Eq. (2), crack growth rate can be estimated and thus crack length can be calculated in both ferrite and austenite. Thus, better service life could be predicted and achieved.

5. Conclusion

Hydrogen emrbittlement in super duplex stainless steels is investigated in this study. Main conclusions are:

- Tensile tests were performed on hydrogen-rich specimens with strain rates from 1.0×10^{-2} to 1.0×10^{-4} s^{-1}. The tensile results show that the ductility is reduced with a decrease in strain rate. The evolution of dislocation density is investigated using in situ neutron diffraction. The results reveal that austenite maintains good plasticity during loading, whilst a loss of plasticity is realised in ferrite.
- Fractography analysis shows that there is a transition from ductile to brittle from surface towards centre across the specimen thickness. In the sample tested at a strain rate of 1.0×10^{-4} s^{-1}, hydrogen embrittlement is absent at depths under 0.27 ± 0.02 mm for austenite, and 0.47 ± 0.09 mm for ferrite. A model is proposed to predict the hydrogen embrittlement in duplex stainless steels, which incorporates hydrogen diffusivity, hydrogen solubility, residual stress, temperature and load. The model describes well the experiment results where the hydorgen embrittlement occurred in ferrite and austenite.
- A model effectively used in this study to describe the experimental results, it could be further developed to assist industrial practice to assess the hydrogen embrittlement, including service life prediction, critical load estimation, and the microstructural design of duplex stainless steels.

Declaration of Competing Interest

The authors declare that they have no known competing financial interests or personal relationships that could have appeared to influence the work reported in this paper.

Acknowledgements

This work was financed by grants HEmS (grant number EP/L014742/1) and DARE (grant number EP/L025213/1) from the UK Engineering and Physical Science Research Council (EPSRC). PEJRDC is grateful to the Royal Academy of Engineering Grant number (RCSRF1718/5/32) for funding a Research Chair. The authors acknowledge the allocation of beam time (RB1620333) at ISIS, Rutherford Appleton Laboratory, funded by the Science and Technology Facilities Council. TWI Ltd., Cambridge is gratefully acknowledged for supplying samples.

References

[1] H.K.D.H. Bhadeshia, R. Honeycombe, Steels Microstructure and Properties, Elsevier, Oxford, 2006.
[2] J.O. Nilsson, Super duplex stainless steels, Mater. Sci. Technol. 8 (8) (1992) 685–700.
[3] K.H. Lo, C.H. Shek, J.K.L. Lai, Recent developments in stainless steels, Mater. Sci. Eng. R 65 (4) (2009) 39–104.
[4] A. Barnoush, M. Zamanzade, H. Vehoff, Direct observation of hydrogen-enhanced plasticity in super duplex stainless steel by means of in situ electrochemical methods, Scr. Mater. 62 (5) (2010) 242–245.
[5] X.Z. Liang, M.F. Dodge, W. Liang, H.B. Dong, Precipitation of chromium nitride nano-rods on lamellar carbides along austenite-ferrite boundaries in super duplex stainless steel, Scr. Mater. 127 (2017) 45–48.
[6] G. Lothongkum, P. Wongpanya, S. Morito, T. Furuhara, T. Maki, Effect of nitrogen on corrosion behavior of 28Cr–7Ni duplex and microduplex stainless steels in air-saturated 3.5 wt% NaCl solution, Corros. Sci. 48 (1) (2006) 137–153.
[7] T. Maki, T. Furuhara, K. Tsuzaki, Microstructure development by thermomechanical processing in duplex stainless steel, ISIJ Int. 41 (6) (2001) 571–579.
[8] H.K.D.H. Bhadeshia, Prevention of hydrogen embrittlement in steels, ISIJ Int. 56 (1) (2016) 24–36.
[9] Y. Deng, A. Barnoush, Hydrogen embrittlement revealed via novel in situ fracture experiments using notched micro-cantilever specimens, Acta Mater. 142 (2018) 236–247.
[10] J. Han, J.-H. Nam, Y.-K. Lee, The mechanism of hydrogen embrittlement in intercritically annealed medium Mn TRIP steel, Acta Mater. 113 (2016) 1–10.
[11] M.A. Stopher, P.E.J. Rivera-Díaz-del-Castillo, Hydrogen embrittlement in bearing steels, Mater. Sci. Technol. 32 (11) (2016) 1184–1193.
[12] B.A. Szost, P.E.J. Rivera-Díaz-del-Castillo, Unveiling the nature of hydrogen embrittlement in bearing steels employing a new technique, Scr. Mater. 68 (7) (2013) 467–470.
[13] A. Turk, D. Bombač, J. Jelita Rydel, M. Zitara, P.E.J. Rivera-Díaz-del-Castillo, E.I. Galindo-Nava, Grain boundary carbides as hydrogen diffusion barrier in a Fe-Ni alloy: A thermal desorption and modelling study, Mater. Des. 160 (2018) 985–998.
[14] M.A. Liu, P.E.J. Rivera-Díaz-del-Castillo, J.I. Barraza-Fierro, H. Castaneda, A. Srivastava, Microstructural influence on hydrogen permeation and trapping in steels, Mater. Des. 167 (2019) 107605.
[15] R. Kirchheim, Reducing grain boundary, dislocation line and vacancy formation energies by solute segregation. i. theoretical background, Acta Mater. 55 (15) (2007) 5129–5138.
[16] M. Hatano, M. Fujinami, K. Arai, H. Fujii, M. Nagumo, Hydrogen embrittlement of austenitic stainless steels revealed by deformation microstructures and strain-induced creation of vacancies, Acta Mater. 67 (2014) 342–353.
[17] V. Venegas, F. Caleyo, J.L. Gonzlez, T. Baudin, J.M. Hallen, R. Penelle, EBSD study of hydrogen-induced cracking in API-5 L-X46 pipeline steel, Scr. Mater. 52 (2) (2005) 147–152.
[18] I.M. Robertson, D. Tetter, Controlled environment transmission electron microscopy, Microsc. Res. Techniq. 42 (4) (1998) 260.
[19] D.F. Teter, I.M. Robertson, H.K. Birnbaum, The effects of hydrogen on the deformation and fracture of β-titanium, Acta Mater. 49 (20) (2001) 4313–4323.
[20] J.G. Morlet, H.H. Johnson, A.R. Troiano, A New Concept of Hydrogen Embrittlement in Steel, Wright Air Development Center, Air Research and Development Command, United States Air Force, 1957.
[21] A.R. Troiano, The role of hydrogen and other interstitials in the mechanical behavior of metals, Trans. ASM 52 (1) (1960) 54–80.
[22] R.A. Oriani, The diffusion and trapping of hydrogen in steel, Acta Metall. 18 (1) (1970) 147–157.
[23] R.A. Oriani, P.H. Josephic, Equilibrium aspects of hydrogen-induced cracking of steels, Acta Metall. 22 (9) (1974) 1065–1074.
[24] R.A. Oriani, A mechanistic theory of hydrogen embrittlement of steels, Berichte der Bunsengesellschaft fr physikalische Chemie 76 (8) (1972) 848–857.
[25] R.A. Oriani, P.H. Josephic, Equilibrium and kinetic studies of the hydrogen-assisted cracking of steel, Acta Metall. 25 (9) (1977) 979–988.
[26] P.J. Ferreira, I.M. Robertson, H.K. Birnbaum, Hydrogen effects on the interaction between dislocations, Acta Mater. 46 (5) (1998) 1749–1757.
[27] I.M. Robertson, P. Sofronis, A. Nagao, M.L. Martin, S. Wang, D.W. Gross, K.E. Nygren, Hydrogen embrittlement understood, Metall. Mater. Trans. B 46 (3) (2015) 1085–1103.
[28] H. Vehoff, W. Rothe, Gaseous hydrogen embrittlement in FeSi- and Ni-single crystals, Acta Metall. 31 (11) (1983) 1781–1793.
[29] D.P. Abraham, C.J. Altstetter, Hydrogen-enhanced localization of plasticity in an austenitic stainless steel, Metall. Mater. Trans. A 26 (11) (1995) 2859–2871.
[30] S. Wang, A. Nagao, P. Sofronis, I.M. Robertson, Hydrogen-modified dislocation structures in a cyclically deformed ferritic-pearlitic low carbon steel, Acta Mater. 144 (2018) 164–176.
[31] M. Connolly, M. Martin, P. Bradley, D. Lauria, A. Slifka, R. Amaro, C. Looney, J.-S. Park, In situ high energy x-ray diffraction measurement of strain and dislocation density ahead of crack tips grown in hydrogen, Acta Mater. 180 (2019) 272–286.
[32] M. Koyama, C.C. Tasan, E. Akiyama, K. Tsuzaki, D. Raabe, Hydrogen-assisted decohesion and localized plasticity in dual-phase steel, Acta Mater. 70 (2014) 174–187.
[33] C. Örnek, P. Reccagni, U. Kiviskk, E. Bettini, D.L. Engelberg, J. Pan, Hydrogen embrittlement of super duplex stainless steel - towards understanding the effects of microstructure and strain, Int. J. Hydrogen Energy 43 (27) (2018) 12543–12555.
[34] X.Z. Liang, M.F. Dodge, S. Kabra, J.F. Kelleher, T.L. Lee, H.B. Dong, Effect of hydrogen charging on dislocation multiplication in pre-strained super duplex stainless steel, Scr. Mater. 143 (2018) 20–24.
[35] M.F. Dodge, M.F. Gittos, H. Dong, S.Y. Zhang, S. Kabra, J.F. Kelleher, In-situ neutron diffraction measurement of stress redistribution in a dissimilar joint during heat treatment, Mater. Sci. Eng. A 627 (2015) 161–170.
[36] T.L. Lee, J. Mi, S. Ren, S. Zhao, J. Fan, S. Kabra, S. Zhang, P.S. Grant, Modelling and neutron diffraction characterization of the interfacial bonding of spray formed dissimilar steels, Acta Mater. 155 (2018) 318–330.
[37] E. Owczarek, T. Zakroczymski, Hydrogen transport in a duplex stainless steel, Acta Mater. 48 (12) (2000) 3059–3070.
[38] N. Kheradmand, R. Johnsen, J.S. Olsen, A. Barnoush, Effect of hydrogen on the hardness of different phases in super duplex stainless steel, Int. J. Hydrogen Energy 41 (1) (2016) 704–712.
[39] B. An, T. Iijima, C. San Marchi, B. Somerday, Micromechanisms of hydrogen-assisted cracking in super duplex stainless steel investigated by scanning probe microscopy, in: ASME 2014 Pressure Vessels and Piping Conference, American Society of Mechanical Engineers, 2014.

[40] J. Song, W.A. Curtin, Atomic mechanism and prediction of hydrogen embrittlement in iron, Nat. Mater. 12 (2) (2013) 145–151.
[41] F. Christien, M.T.F. Telling, K.S. Knight, Neutron diffraction in situ monitoring of the dislocation density during martensitic transformation in a stainless steel, Scr. Mater. 68 (7) (2013) 506–509.
[42] B. Kim, E. Boucard, T. Sourmail, D. San Martn, N. Gey, P.E.J. Rivera-Daz-del Castillo, The influence of silicon in tempered martensite: understanding the microstructure–properties relationship in 0.5–0.6 wt. c steels, Acta Mater. 68 (2014) 169–178.
[43] G.H. Zhao, X.Z. Liang, B. Kim, P.E.J. Rivera-Díaz-del-Castillo, Modelling strengthening mechanisms in beta-type ti alloys, Mater. Sci. Eng. A 756 (2019) 156–160.
[44] A. Yousefi, G. Itoh, Tensile properties of an electrolytically hydrogen charged duplex stainless steel affected by strain rate, ISIJ Int. 58 (3) (2018) 561–565.
[45] J. Song, W. Curtin, A nanoscale mechanism of hydrogen embrittlement in metals, Acta Mater. 59 (4) (2011) 1557–1569.
[46] V. Olden, C. Thaulow, R. Johnsen, Modelling of hydrogen diffusion and hydrogen induced cracking in supermartensitic and duplex stainless steels, Mater. Des. 29 (10) (2008) 1934–1948.
[47] X. Zhou, D. Marchand, D.L. McDowell, T. Zhu, J. Song, Chemomechanical origin of hydrogen trapping at grain boundaries in fcc metals, Phys. Rev. Lett. 116 (7) (2016) 075502.
[48] V. Olden, A. Saai, L. Jemblie, R. Johnsen, FE simulation of hydrogen diffusion in duplex stainless steel, Int. J. Hydrogen Energy 39 (2) (2014) 1156–1163.
[49] A. Pineau, A.A. Benzerga, T. Pardoen, Failure of metals i: brittle and ductile fracture, Acta Mater. 107 (2016) 424–483.
[50] Recommended practice DNVGL-RP-F112 duplex stainless steel - design against hydrogen induced stress cracking (2018).